# Plastic Forming of Graphene Oxide Membranes into 3D Structures

Siyu Liu, Marta Cerruti, and Francois Barthelat*

Cite This: *ACS Nano* 2020, 14, 15936−15943

Read Online

ACCESS | Metrics & More | Article Recommendations | Supporting Information

**ABSTRACT:** Flat, membrane-like materials made of graphene oxide (GO) nanoflakes have extraordinary mechanical properties including high stiffness, high strength, and low weight. However, the forming of complex nonplanar structures from flat GO membranes is difficult because of the intrinsic brittleness of GO. Here we present a simple and low-cost method to plasticize vacuum-filtrated GO membranes using a cellulose additive. Compared with the pure GO membrane, the GO−cellulose membranes had a lower Young's modulus but significantly improved ductility. Using the flat GO−cellulose membrane, we successfully embossed hemispherical caps with high geometrical fidelity, smooth surfaces, and no tearing or other damages to the membrane. The stiffness of the embossed 3D structure was increased further by cross-linking with a borax solution. Hemispherical caps made of 75 wt % GO with 25 wt % cellulose slurry combining borax cross-linking showed the highest stiffness. This study extends the applications of GO membranes and allows the harnessing of their extraordinary properties to nonplanar structures.

**KEYWORDS:** *graphene oxide, nanoflakes, cellulose slurry, embossing, high stiffness, 3D structures*
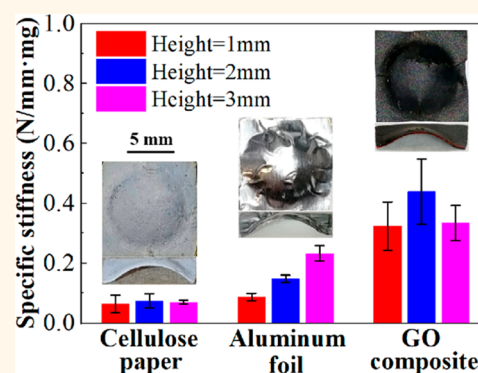
Free-standing graphene oxide (GO) membranes are attractive structural materials due to their high stiffness, high strength, and low weight. However, they are very brittle, and the reported elongation of GO membranes or reduced GO membranes is below 1%,[1−3] which is on the same order of magnitude of ceramics and glasses. The brittleness of GO comes from the limited movement and multiplication of topological defects.[4] Stone−Wales defects in the hexagonal lattice of GO can be regarded as edge dislocation dipoles, but they are tightly bonded and cannot move as easily as dislocations in metals for plastic deformation.[5,6] Flat GO membranes have broad applications as acoustic diaphragms,[7,8] gas sieving,[9] flexible electronics,[10−12] and energy devices,[13] and more elaborated designs that include nonplanar features would greatly extend the range of these applications. The inherent brittleness of GO membranes however makes it impossible to form into 3D structures without tearing or cracking, and there is therefore a need to improve their ductility. Several factors govern the ductility of GO. The first one is the relative amount of different oxygen-containing functional groups on GO. GO flakes with a high amount of epoxide groups have a higher failure strain than those with fewer epoxide groups, because of an epoxide-to-ether transformation that dissipates strain energy and hinders crack propagations.[14−16] Loading condition is another factor: GO membranes are more brittle at higher strain rate and can undergo a ductile to brittle transition when strain

rate increases from 0.01% s$^{-1}$ to 0.1% s$^{-1}$.[17] This rate-dependent plasticity originates from the sliding of layers with frictional stick−slip motions produced by the interactions among the functional groups.[17] Finally environmental effects such as humidity can also influence ductility of GO membranes. GO is susceptible to water plasticization due to the restacking of GO nanoflakes in wet conditions, a phenomenon that can be used to control deformation pathways and failure mechanisms to make solid structures.[18−20] However, most of these effects were observed at the nanoscale and only improved ductility of a single GO flake or a few layers of stacked GO flakes. How these nanoscale effects translate to, and can be harnessed in macroscale membranes is not fully understood. Another approach to increase ductility of GO membranes could be the addition of plasticizers. Phthalates, phosphates, adipates, benzoates, and epoxidized fatty acid esters are plasticizers that are commonly used for polymers, but these additives have limitations such as high volatility, flammability, compatibility with other materials,
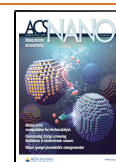
health hazards, and environmental effects.[21] There are no reports about enhancing ductility of GO membranes using these common plasticizers, possibly due to difficulty in creating homogenous dispersions. Because of the limited ductility of GO-based materials, there are only a few reports of nonplanar GO or GO-based composite structures. Reported methods include origami and kirigami methods to fold-and-paste GO or reduced GO structures such as coils and cross-signs made of GO membranes,[19] paper airplanes made of poly(acrylic acid-*co*-(4-acrylamidophenyl)boronic acid) reinforced GO membranes[22] or reduced GO−cellulose composites,[23] and cranes and twisted knots made by reduced GO membranes.[24] However, these methods cannot create irregular curved surfaces, and the final dimensions of the product are not fully controlled. Also no mechanical tests were reported on these folded or pasted structures, so the folding process weakening the GO membrane remains a likely possibility. A prime candidate forming method to process GO membrane into 3D structure is embossing, a widely used method to manufacture metal sheets into high-precision mechanical parts for daily appliances, the automobile industry, and aerospace. In the embossing process, out-of-plane shapes are created from a thin and flat workpiece using shaped tools pressed together.[25] In this study we extended the embossing technique to GO membranes using cellulose. Cellulose is one of the most abundant and renewable biopolymers.[26] A pristine GO suspension presents a good dispersion when mixing with cellulose,[27] and GO flakes can spread on the porous cellulose skeleton.[28,29] The long-chain structure of cellulose fibers can prevent crack generation and propagation in the matrix material.[30] We hypothesize therefore that cellulose can improve ductility and formability of GO membranes.

## RESULTS AND DISCUSSION

**Fabrication and Characterization of GO−Cellulose Membranes.** Fabrication (Figure 1) started by soaking
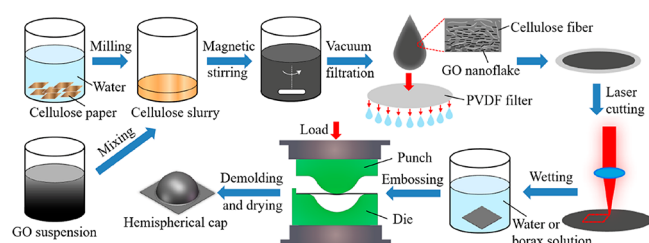


**Figure 1.** Fabrication steps for the GO−cellulose hemispherical cap.

cellulose paper in water for 24 h to make it softer, followed by milling for 10 min to obtain a uniform cellulose slurry (Supporting Information, Figure S1a). The length of the cellulose fibers in the slurry was in the ∼100−2600 $\mu$m range (Supporting Information, Figures S1b,c). A GO suspension was then prepared by dissolving a GO paste in water to produce a suspension with a concentration of 10 mg mL$^{-1}$. We then mixed the GO suspension with the cellulose slurry; these two components were well dispersed and mixed after magnetic stirring for 24 h (Supporting Information, Figure S1d). Finally we poured the mixed suspension on a hydrophilic PVDF filter membrane mounted on a vacuum chamber (−635 mmHg). We dried the GO−cellulose membrane in air while still maintaining vacuum in the filtration system and peeled it from

the filter membrane manually after 24 h for the pure GO membrane and after 10 h for all the cellulose-containing membranes (the preparation that included a cellulose slurry had faster filtration rates, which may have been due to the cellulose fibers permeating through the GO nanoflakes[31,32] and allowing water to filter through it faster). With a fixed mass of 0.56 g, we prepared five membranes with different GO and cellulose concentrations: (i) 100 wt % GO; (ii) 75 wt % GO with 25 wt % cellulose; (iii) 50 wt % GO with 50 wt % cellulose; (iv) 25 wt % GO with 75 wt % cellulose; and (v) 100 wt % cellulose.

The GO suspension showed acidity because of the carboxyl groups at the edges of GO nanoflakes, while the addition of cellulose increased the pH value slightly (Supporting Information, Figure S2, the pH value ranged from 1.74 ± 0.04 to 2.26 ± 0.02). The pH value mainly influences the dispersion of GO: under highly basic conditions (pH = 14), individual GO nanoflakes prefer to dissolve and disperse more uniformly in water like a regular salt.[33,34] But in our study, the suspension was still under highly acidic conditions (pH < 3) even after adding the cellulose, so this small pH change likely did not change the way GO nanoflakes self-assembled during membrane formation. The resulting GO−cellulose membranes were flat and smooth, and the color ranged between black (75 wt % GO, Figure 2a) and brown (25 wt % GO, Figure 2b). The density of the materials ranged from 0.65 ± 0.05 g cm$^{-3}$ to 1.48 ± 0.02 g cm$^{-3}$, the densest materials having the highest GO concentration (Figure 2c). The thickness ranged between 86 ± 2 and 185 ± 6 $\mu$m, with thicker samples obtained in samples with high cellulose concentration (Figure 2c). From the scanning electron microscopy (SEM) image of the sample surface, the pure GO membrane looked dense (Figure 2d); the 75 wt % GO membrane (Figure 2e) also looked relatively dense, with needle-like cellulose fibers entangled and distributed randomly between GO. In contrast, the 50 wt % (Figure 2f) and the 25 wt % (Figure 2g) GO membranes were less dense and showed many small pores under SEM. In order to image the cross-section, we cut the samples with a razor blade after immersing in liquid nitrogen, which created smooth cross-sectional cuts. From the cross-section image of the 25 wt % GO membrane (Figure 2h), individual GO nanoflakes or cellulose fibers cannot be distinguished under SEM, most likely because the two components were intimately fused with each other. We found no evidence of aggregation, *i.e.*, regions with distinct morphologies. We could visualize cellulose fibers if we broke the samples by hand rather than cutting them: in this case pulled out cellulose fibers protruded from the cross-section, and we clearly observed their homogenous distribution throughout the cross-section (Supporting Information, Figure S3). We also performed energy dispersive spectroscopy (EDS) on the 75 wt % GO membrane (Supporting Information, Figure S4) across the cross-section and detected a small amount (less than 1.5%) of Ca, N, S, Cl, Na, and Al. These elements possibly came from $CaSO_4 \cdot 2H_2O$, $C_{10}H_{16}N_2O_8$, $Na_2S$, $ClO_2$, and $Al_2(SO_4)_3 \cdot 18H_2O$ present in cellulose paper (Supporting information, Table S1). The uniform distribution of these elements also reflected the uniform dispersion of GO nanoflakes and cellulose fibers in the filtrated membrane.

**Mechanical Properties of GO−Cellulose Membranes.** We measured the mechanical properties of the GO−cellulose membranes using a three-point bending configuration. Figure 3a shows typical flexural stress−strain curves for GO−cellulose membranes with different compositions. Pure GO membranes
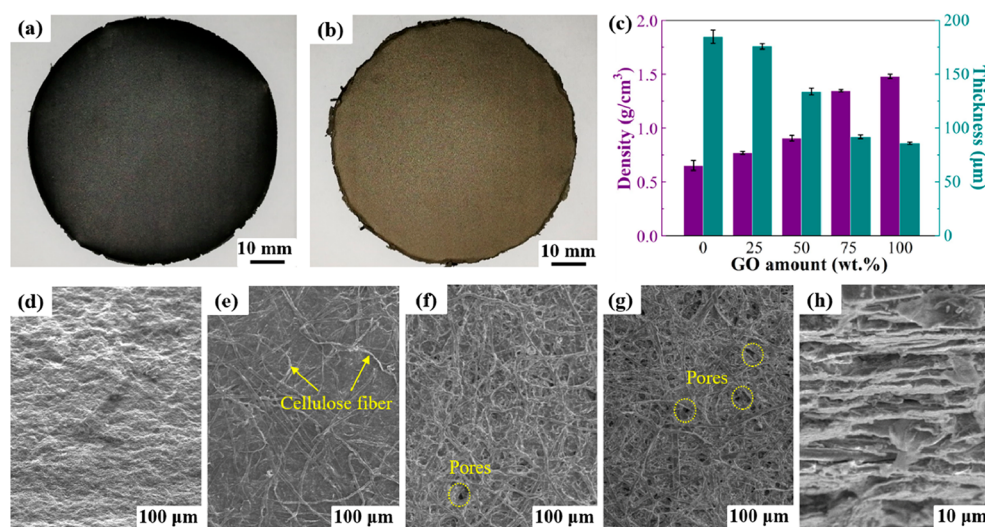
**Figure 2.** Morphology of the GO–cellulose membrane: optical image of (a) the 75 wt % GO membrane and (b) the 25 wt % GO membrane; (c) density and thickness of the GO–cellulose membranes with different GO amounts; (d–g) SEM images of the surface of the 100, 75, 50, and 25 wt % GO membranes; (h) SEM image of the cross-section of the 25 wt % GO membrane.
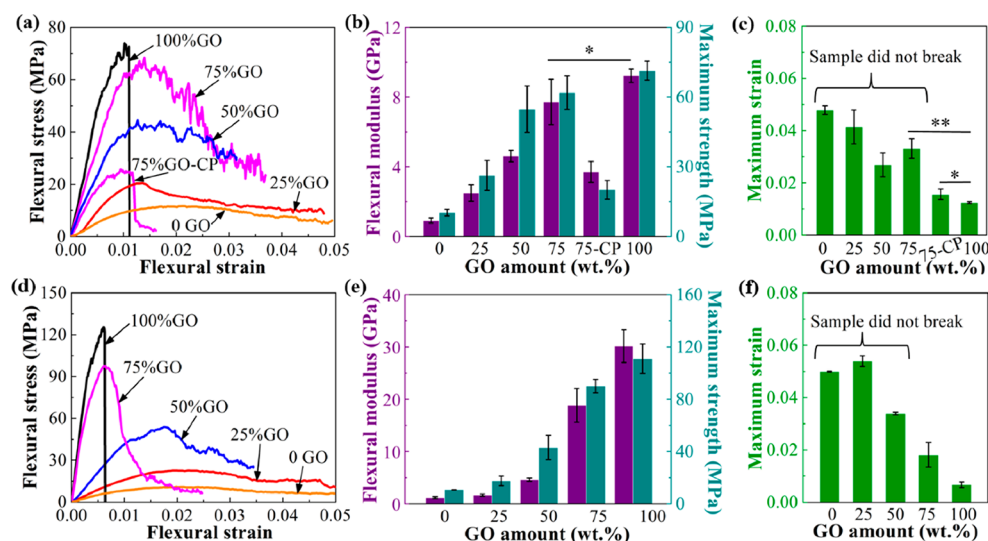


**Figure 3.** Flexural tests on GO–cellulose membranes: (a) flexural stress–strain curve, (b) flexural modulus and maximum flexural strength, and (c) maximum flexural strain of the as-prepared GO membranes; (d) flexural stress–strain curve, (e) flexural modulus and maximum flexural strength, and (f) maximum flexural strain of the borax cross-linked GO membranes. The results are shown as a function of GO amount. 75-CP indicates a sample made with the pure cellulose powder; all other samples were prepared with a milled cellulose slurry. Error bars indicate the standard deviations. n.s.: not significant, *: $p < 0.1$, **: $p < 0.01$.

were the stiffest and strongest, but also the most brittle. The addition of cellulose decreased the modulus and strength, but also greatly improved ductility. The samples with cellulose were so ductile that they could not be broken with the three-point bending configuration used here and instead slipped out of the fixture. Figure 3b,c show how the flexural modulus, maximum flexural stress, and maximum strain changed as a function of composition. For example, the 75 wt % GO membrane retained 85% of flexural modulus but showed around three times larger fracture strain than the pure GO membrane. To understand the reason for the increased ductility induced by the addition of a cellulose slurry, we also compared the effect of the milled cellulose slurry and the pure cellulose powder. We fabricated a similar membrane with 75 wt % of GO and 25 wt % of pure cellulose powder using the same procedure (sample called 75-CP in Figure 3). The results

(Figures 3a–c) show that flexural modulus, strength, and strain at breaking all decreased when using the pure cellulose powder. Although the pure cellulose powder improved membrane ductility compared to pure GO, the improvement was lower than that achieved by using the milled cellulose slurry. We hypothesize that this was mainly because our prepared cellulose slurry had longer fibers than the pure cellulose powder (size distribution for the milled cellulose slurry: ~100–2600 μm, Figure S1; for the commercial cellulose powder: ~50–350 μm, from the manufacturer's specifications). The cellulose fibers probably generated a crack-bridging mechanism, where the cellulose fibers can delay or prevent crack propagation under the flexural load: short cellulose fibers were only effective to bridge microcracks and prevent them from growing into macrocracks, while long fibers can also bridge larger cracks and absorb energy through friction

between GO and cellulose fibers (Supporting Information, Figure S5).[30,35] Therefore, longer cellulose fibers can resist higher stresses; they are more robust and tougher and provide the GO membrane with improved ductility.

We also explored a borax cross-linking method to make the GO−cellulose membranes stiffer and stronger. The widely used cross-linking method requires mixing the GO suspension and the borax solution before filtration. Borate ions can react with hydroxyl groups on the GO surface to form borate orthoesters.[36] The formation of these covalent bonds made the GO membrane stiffer and stronger but also more brittle because these covalent bonds cannot be readily re-formed once broken.[36] To overcome this obstacle to properly embossing the material, we cross-linked the GO−cellulose membrane in borax solution after filtration. We prepared a borax solution by dissolving borax $(Na_2B_4O_7 \cdot 10H_2O)$ powder in water using magnetic stirring at 70 °C for 30 min. Then we immersed the GO−cellulose membrane in the borax solution (0.1 mol $L^{-1}$) for 10 seconds and dried it in air for 24 h. Figure 3d shows the flexural stress−strain curve of the borax cross-linked GO−cellulose membrane, and Figure 3e,f compare the flexural modulus and maximum flexural stress and strain, respectively. This cross-linking method only worked for the pure GO membrane or GO−cellulose membrane with a high GO amount. After cross-linking, the flexural modulus showed no change when GO was lower than 50 wt %, while the flexural modulus of the 75 wt % GO membrane and the pure GO membrane increased by 1.5 ± 0.2 and 2.3 ± 0.2 times, respectively, compared to the results obtained without cross-linking. To explain these results, we need to consider that although borax can crosslink both GO and cellulose through the reaction of borate ions with hydroxyl groups,[37,38] the reaction requires the hydroxyl groups to be close enough to form bonds. It is reported that the formation of hydrogen bonds between cellulose fibers needs the distance of adjacent hydroxyl groups in the range of 0.25 to 0.35 nm.[39] However, from our SEM results (Figure 2), the addition of cellulose induced micron-sized pores; so very likely, the hydroxyl groups on cellulose fibers were not close enough for cross-linking. In a composite membrane with low GO concentration, the GO nanoflakes were dispersed within a cellulose matrix, and thus most of the GO was also not close enough to each other. This led to few cross-links created in the low-GO sample and thus no significant changes in flexural modulus and strength upon borate reaction.

**Embossing 3D GO Structures.** We explored how the GO−cellulose nanocomposite membrane can be formed into 3D structures (here a hemispherical cap) using an embossing technique. We manufactured embossing tools by 3D printing as shown in Figure 4a. Figure 4b shows a schematic of a cross-section for the assembled embossing tools that highlights the hemispherical profile of the tool, as well as two key design elements: (i) raised shoulders at the edge of the tool for alignment and (ii) fillets near the flange to minimize stress concentrations during embossing. We cut 10 mm × 10 mm squares off the GO−cellulose membrane and soaked the square in water for 10 seconds to disrupt hydrogen bonds, making it softer and more malleable. We then placed the wet membrane in the embossing tool and applied pressure manually. The closed setup was fixed by flat-nose pliers and dried in air for 24 h, during which the hydrogen bonds re-formed, effectively sealing the 3D geometry. Finally, the embossing tools were separated and the embossed GO−
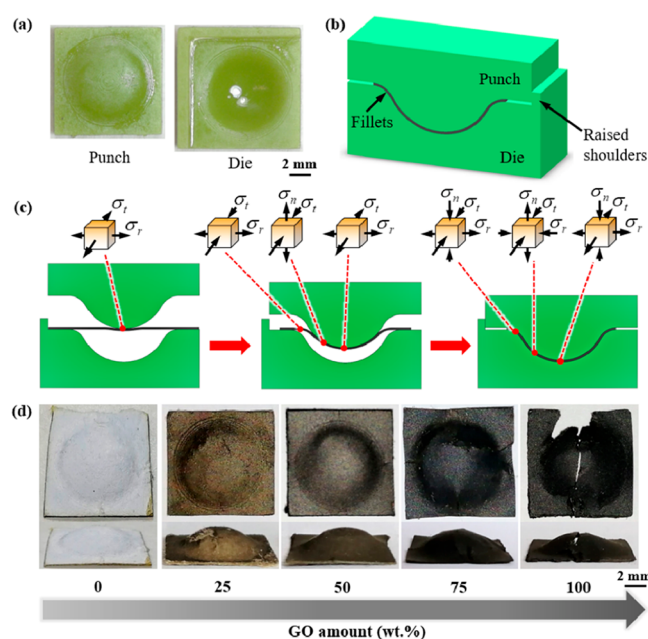


Figure 4. Embossing process of the GO−cellulose nanocomposite membrane: (a) photographs of the 3D-printed embossing tools; (b) schematic of the assembled embossing tools in the middle cross-section; (c) stress condition of different regions during the embossing process ($\sigma_t$, $\sigma_r$, and $\sigma_n$ represent the circumferential stress, the radial stress, and the vertical stress, respectively); (d) optical images of the embossed hemispherical caps with different GO amounts.

cellulose structure was simply peeled from the tools. The samples with cellulose were recovered intact, but pure GO samples were heavily damaged during the embossing process. To better understand the failure patterns of these materials, it is useful to consider the state of stress experienced by the membrane during embossing. Figure 4c shows the stress state that develops in different regions of the sheet during the embossing process. The middle area was under biaxial tensile stresses (circumferential stress $\sigma_t$ and radial stress $\sigma_r$) at the initial stage, with the addition of a compressive vertical stress ($\sigma_n$) when the punch contacted with the die. The sidewall bore a tensile $\sigma_n$ and a compressive $\sigma_t$ during the embossing process and another compressive $\sigma_r$ when the sample touched the die. Similar to the sidewall, the flange had a tensile $\sigma_r$ and a compressive $\sigma_t$, with an extra compressive $\sigma_n$ when the tools were closed. The whole sample was under a complex triaxial stress state at the final stage. Figure 4d shows images of the embossed hemispherical caps. The pure GO cap had broken areas and showed long cracks along the radial direction. The compressive $\sigma_t$ at the sidewall caused these cracks to form when the membrane was stretched from a larger to a smaller diameter during the embossing process. In contrast, the GO−cellulose embossed sheets looked undamaged, smooth, and compact. In order to characterize the geometrical accuracy of the structure, we cut the hemispherical cap in the middle using precision laser cutting and observed the cross-sections (Supporting Information, Figure S6). The cross-section of each sample was almost matched with the targeted shape, which indicated the high accuracy of the embossed caps. The GO−cellulose caps contained only a few small wrinkles (Supporting Information, Figure S7) along the radial direction,
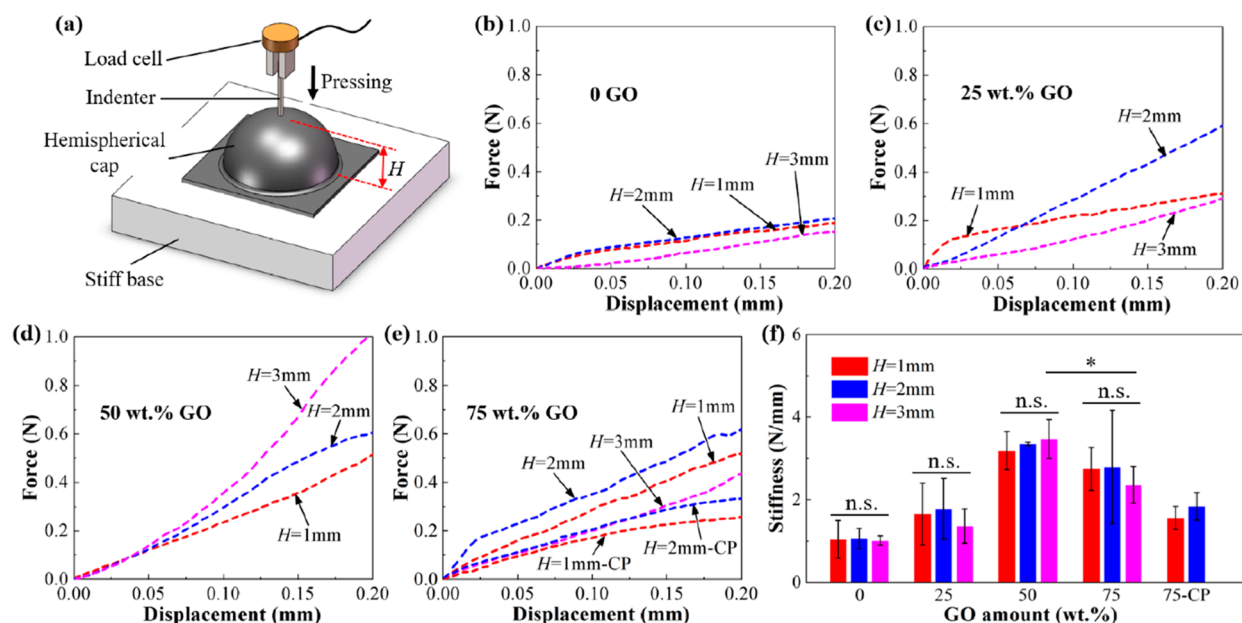
**Figure 5.** Stiffness test on the embossed hemispherical caps using a compressive point force in the center: (a) schematic of the experimental setup; (b−e) force−displacement curves with the GO amount of 0, 25, 50, and 75 wt %, respectively; (f) summary of stiffness for different GO amounts and sample heights $H$. 75-CP indicates a sample made with pure cellulose powder; all other samples were prepared with a milled cellulose slurry. Error bars indicate the standard deviations. n.s.: not significant, *: $p < 0.1$, **: $p < 0.01$.
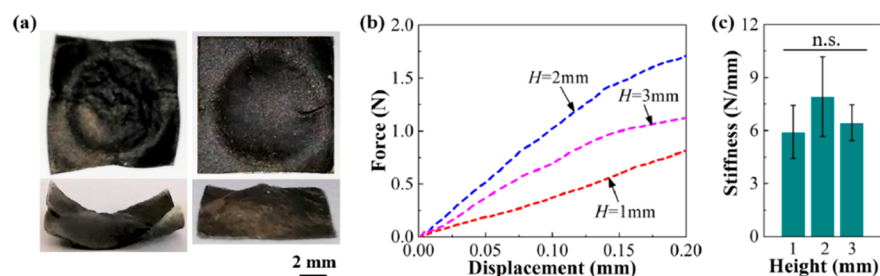


**Figure 6.** Borax cross-linking of the GO−cellulose hemispherical cap: (a) optical image of the borax cross-linked 75 wt % GO caps (left side: cross-linking after embossing; right side: cross-linking during embossing); (b) force−displacement curve of the borax cross-linked 75 wt % GO cap under a compressive point force in the center; (c) stiffness of the 75 wt % GO cap after cross-linking. $H$ represents the height of the hemispherical cap.

without any observed cracks at the apex region (Supporting Information, Figure S8).

**Mechanical Properties of the 3D GO Structures.** Using a point force in the center (Figure 5a), we measured the stiffness of embossed sheets with 0, 25, 50, and 75 wt % GO, with a height of the hemispherical cap ($H$) of 1, 2, and 3 mm, respectively. The pure GO sheets, heavily damaged from embossing, were not tested. Figure 5b−e show the corresponding force−displacement curves, and Figure 5f summarizes the stiffness calculated from the slope of the force−displacement curves. The 50 wt % GO hemispherical cap showed the highest average stiffness, while the 75 wt % GO cap had a slightly decreased stiffness (only statistically different for the $H$ = 3 mm). This result indicates that there is an optimum concentration of cellulose fibers: too many cellulose fibers induce pores and disorder in the membrane, but on the other end too few fibers have no toughening effect with effective properties closer to pure GO membranes, which are brittle. The stiffness of the 75 wt % GO caps made with pure cellulose powder (Figure 5e) was also lower than that measured on samples made using the milled cellulose slurry; in fact, the $H$ = 3 mm cap could not be formed using pure

cellulose powder because of large cracks. Our results did not show statistically different stiffness values as a function of height for any amount of GO tested.

We also used the 75 wt % GO (with milled cellulose slurry) hemispherical cap as the sample to test increasing stiffness using borax cross-linking. We immersed the already embossed 75 wt % GO cap in the borax solution for 10 seconds to cross-link and then dried it in air. However, the cap collapsed and was not able to maintain its 3D configuration upon drying (Figure 6a, left side). We improved the fabrication process by immersing the flat membrane in the borax solution (for 10 seconds) and then embossed it immediately when the sample was still wet. As in the previous embossing procedure, we peeled the cap from the tools after 24 h of drying. The cap made with this method was able to maintain its configuration and looked compact (Figure 6a, right side). For the first method, the wet sample became heavier after absorbing the borax solution, and since it was already removed from the embossing tools, there was no underlying support to help the membrane carry the extra weight, causing it to collapse. We found the 3D sample collapsed after immersing in both water and borax solution if it was left without the support from the
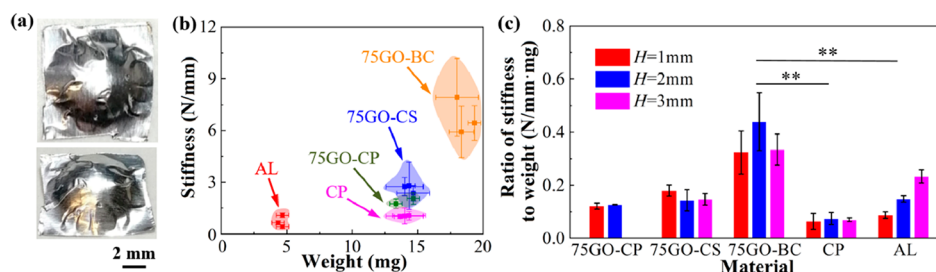
**Figure 7.** Summary of stiffness and weight of the hemispherical caps made of different materials: (a) optical image of an embossed aluminum cap; (b) comparison of the stiffness and weight; (c) comparison of the ratio of stiffness to weight. $H$ represents the height of the hemispherical cap. Error bars indicate the standard deviations. n.s.: not significant, *: $p < 0.1$, **: $p < 0.01$.

embossing tools. The second method can overcome this problem by applying continuous pressure through the embossing tools. The embossing tools can hold the wet sample and keep it stretched to prevent shrinking before it is completely dried. Using this improved method, we fabricated and tested the stiffness of the cross-linked 75 wt % GO caps with the $H$ from 1 mm to 3 mm. Figure 6b shows the force–displacement curve, and Figure 6c shows the stiffness values of the cross-linked caps. After cross-linking, the stiffness of the $H$ = 1 mm, $H$ = 2 mm, and $H$ = 3 mm cap increased by $1.2 \pm 0.5$, $1.8 \pm 0.8$, and $1.7 \pm 0.5$ times, respectively. The $H$ = 2 mm cap had the highest average stiffness of $8 \pm 2$ N mm$^{-1}$ among all the samples. We finally tested the stiffness of the 75 wt % GO cap under cyclic loading both before (Supporting Information, Figure S9) and after borax cross-linking (Supporting Information, Figure S10). The caps were able to keep their high stiffness after 10 cycles of loading and unloading, which indicated the samples were stable and can work for the applications where cyclic loading conditions are need.

## CONCLUSION

In this study we developed a feasible method to enhance ductility of GO nanoflake membranes. This method used a recyclable cellulose slurry milled from cellulose paper as an additive and used water as the solvent for the whole fabrication process. The filtered nanocomposite membrane showed uniformly dispersed cellulose fibers and GO across the cross-section. After mixing 25 wt % of the cellulose slurry with 75 wt % of GO, the filtered membrane retained 85% of the Young's modulus but showed around three times larger flexural fracture strain than the pure GO membrane. Using the GO–cellulose membrane, we successfully formed hemispherical caps with high accuracy and smooth and compact surfaces by an embossing method. We also improved the stiffness of the cap further by immersion cross-linking in a borax solution. Figure 7 shows an overview of the properties in terms of stiffness and weight with comparison with similar caps made of aluminum foils (thickness 16 $\mu$m, Figure 7a and Supporting Information, Figure S11). The stiffness, weight, and stiffness to weight ratio of the caps made of different materials are summarized in Figures 7b,c. The abbreviations in the figure are 75GP-CP for the 75 wt % GO with pure cellulose powder, 75GO-CS for the 75 wt % GO with milled cellulose slurry, 75GO-BC for the 75 wt % GO with cellulose slurry and borax cross-linking, CP for the cellulose paper, and AL for the aluminum foil. The 75GO-BC cap shows not only significantly higher stiffness to weight ratios than other GO-containing samples but also higher ratios than CP and AL. The GO–cellulose hemispherical cap we made has high stiffness, low weight, and high dimensional

precision, which greatly extended the applications of flat GO membranes where nonplanar structures are required.

## MATERIALS AND METHODS

**Materials.** Graphene oxide pastes were used as received from Abalonyx Innovative Materials (product number 1.2A). The raw GO paste was the same product as in our previous study:[40] the overall size of GO flakes was 1−25 $\mu$m (median value 5 $\mu$m); the atomic percentage of carbon was $64.3 \pm 0.5\%$, and oxygen was $35.0 \pm 0.3\%$, as measured by X-ray photoelectron spectroscopy (XPS using a monochromatic Al K$\alpha$ photoelectron spectrometer, Thermo Scientific); the relative amounts of C−C, C−O, and C═O bonds and aromatic C bonds ($\pi$−$\pi$* shake-up band) were $54 \pm 3\%$, $35 \pm 2\%$, $10.3 \pm 0.3\%$, and $0.4 \pm 0.3\%$, respectively, as calculated from C 1s high-resolution XPS spectra (Supporting Information, Figure S12). The GO paste only contained small amounts of N (1%) and Si (0.4%) detected on one out of three spots by XPS. Cellulose paper was obtained from Studio Notebook (product number 05-0502657). Pure cellulose powder (product number C6288) and borax powder (product number 221732) were both acquired from Sigma-Aldrich. PVDF filter membranes with 90 mm diameter and 0.22 $\mu$m pore size were also acquired from Sigma-Aldrich.

**Morphology Characterizations.** Surface and cross-section morphologies of GO−cellulose membranes were characterized using an environmental scanning electron microscope (FEI Quanta 450 FE-ESEM), with an accelerating voltage of 10 kV under a low-vacuum mode. Morphologies of embossed hemispherical caps were characterized using an optical microscope (BX-51M, Olympus).

**pH, Thickness, and Density Measurements.** The pH value of the mixed GO and cellulose suspension was measured by a digital pH meter (Orion 3-star Benchtop pH meter, Fisher Scientific). The pH value of each suspension was recorded after it became stable for more than five seconds. The thickness of the filtrated GO−cellulose membranes was measured by a digital micrometer. For the same membrane, the thickness was measured at five different locations, and the average value was reported. The mass of the membrane was measured by a high-resolution balance scale (Mettler Toledo), and the density was calculated from the ratio of mass to volume.

**Mechanical Tests.** Samples for mechanical tests were cut from the membranes using a precision laser (model Vitrolux, Vitro Laser Solutions UG) with a power of 354.8 mW and a wavelength of 355 nm. Laser cutting ensured precise control of the sample geometry and dimensions. Three-point bending tests were performed on a miniature loading stage (Ernest F. Fullam, Inc) equipped with a 20 g load cell. The sample was loaded at a quasi-static rate of 0.02 mm/s until complete failure or until the sample slipped out of the fixture. The sample size for the three-point bending test was a 20 mm × 2 mm rectangular strip. The stiffness of embossed structures was tested using a point force in the center. This test was performed on the same loading stage with the flexural test but equipped with a 10 lb load cell. The embossed structures were placed on a flat and stiff base, with an indenter slowly (0.01 mm/s) pressing the center of the sample. Force−displacement curves were reported for this test.

**3D Printing.** Embossing tools were manufactured by a high-resolution 3D printer (Micro HiRes Machine, EnvisionTech) based on digital light processing technology using an acrylonitrile butadiene styrene (ABS) polymer (3DM-XGreen, EnvisionTech Perfactory). The sequential laser in the 3D printer cured the thin polymer layer through photopolymerization to achieve layer-by-layer 3D printing. After this process, the printed sample was transferred into a post-curing light pulsing chamber (Otoflash curing unit) for hardening. The printed embossing tools had smooth surfaces, fully dense structures, and high-fidelity geometries.

## ASSOCIATED CONTENT

### Ⓢ Supporting Information

The Supporting Information is available free of charge at https://pubs.acs.org/doi/10.1021/acsnano.0c07344.

Additional figures and a table (PDF)

## AUTHOR INFORMATION

### Corresponding Author

**Francois Barthelat** − *Department of Mechanical Engineering, McGill University, Montreal, QC H3A 2K6, Canada; Department of Mechanical Engineering, University of Colorado, Boulder, Colorado 80309, United States;* ⓘ orcid.org/0000-0001-8393-3612; Email: francois.barthelat@colorado.edu

### Authors

**Siyu Liu** − *Department of Mechanical Engineering, McGill University, Montreal, QC H3A 2K6, Canada*

**Marta Cerruti** − *Department of Mining and Materials Engineering, McGill University, Montreal, QC H3A 0C5, Canada;* ⓘ orcid.org/0000-0001-8533-3071

Complete contact information is available at:
https://pubs.acs.org/10.1021/acsnano.0c07344

### Notes

The authors declare no competing financial interest.

## ACKNOWLEDGMENTS

## REFERENCES

(1) Dikin, D. A.; Stankovich, S.; Zimney, E. J.; Piner, R. D.; Dommett, G. H.; Evmenenko, G.; Nguyen, S. T.; Ruoff, R. S. Preparation and Characterization of Graphene Oxide Paper. *Nature* **2007**, *448*, 457−460.

(2) Park, S.; Lee, K.; Bozoklu, G.; Cai, W.; Nguyen, S. T.; Ruoff, R. S. Graphene Oxide Papers Modified by Divalent Ions-Enhancing Mechanical Properties *via* Chemical Cross-Linking. *ACS Nano* **2008**, *2*, 572−578.

(3) Chen, H.; Müller, M. B.; Gilmore, K. J.; Wallace, G. G.; Li, D. Mechanically Strong, Electrically Conductive, and Biocompatible Graphene Paper. *Adv. Mater.* **2008**, *20*, 3557−3561.

(4) Warner, J. H.; Margine, E. R.; Mukai, M.; Robertson, A. W.; Giustino, F.; Kirkland, A. I. Dislocation-Driven Deformations in Graphene. *Science* **2012**, *337*, 209−212.

(5) Ertekin, E.; Chrzan, D. C.; Daw, M. S. Topological Description of the Stone-Wales Defect Formation Energy in Carbon Nanotubes and Graphene. *Phys. Rev. B: Condens. Matter Mater. Phys.* **2009**, *79*, 155421.

(6) Chen, S.; Chrzan, D. C. Continuum Theory of Dislocations and Buckling in Graphene. *Phys. Rev. B: Condens. Matter Mater. Phys.* **2011**, *84*, 214103.

(7) Tian, H.; Li, C.; Mohammad, M. A.; Cui, Y.; Mi, W.; Yang, Y.; Xie, D.; Ren, T. Graphene Earphones: Entertainment for Both Humans and Animals. *ACS Nano* **2014**, *8*, 5883−5890.

(8) Woo, S. T.; Han, J.; Lee, J. H.; Cho, S.; Seong, K.; Choi, M.; Cho, J. Realization of a High Sensitivity Microphone for a Hearing Aid Using a Graphene-PMMA Laminated Diaphragm. *ACS Appl. Mater. Interfaces* **2017**, *9*, 1237−1246.

(9) Shen, J.; Liu, G.; Huang, K.; Chu, Z.; Jin, W.; Xu, N. Subnanometer Two-Dimensional Graphene Oxide Channels for Ultrafast Gas Sieving. *ACS Nano* **2016**, *10*, 3398−3409.

(10) Soni, M.; Kumar, P.; Pandey, J.; Sharma, S. K.; Soni, A. Scalable and Site Specific Functionalization of Reduced Graphene Oxide for Circuit Elements and Flexible Electronics. *Carbon* **2018**, *128*, 172−178.

(11) Zarrin, H.; Sy, S.; Fu, J.; Jiang, G.; Kang, K.; Jun, Y.; Yu, A.; Fowler, M.; Chen, Z. Molecular Functionalization of Graphene Oxide for Next-Generation Wearable Electronics. *ACS Appl. Mater. Interfaces* **2016**, *8*, 25428−25437.

(12) He, Q.; Wu, S.; Gao, S.; Cao, X.; Yin, Z.; Li, H.; Chen, P.; Zhang, H. Transparent, Flexible, All-Reduced Graphene Oxide Thin Film Transistors. *ACS Nano* **2011**, *5*, 5038−5044.

(13) Choi, B. G.; Huh, Y. S.; Park, Y. C.; Jung, D. H.; Hong, W. H.; Parkd, H. S. Enhanced Transport Properties in Polymer Electrolyte Composite Membranes with Graphene Oxide Sheets. *Carbon* **2012**, *50*, 5395−5402.

(14) Wei, X.; Mao, L.; Soler-Crespo, R. A.; Paci, J. T.; Huang, J.; Nguyen, S. T.; Espinosa, H. D. Plasticity and Ductility in Graphene Oxide Through a Mechanochemically Induced Damage Tolerance Mechanism. *Nat. Commun.* **2015**, *6*, 8029.

(15) Hou, Y.; Zhu, Y.; Liu, X.; Dai, Z.; Liu, L.; Wu, H.; Zhang, Z. Elastic-Plastic Properties of Graphene Engineered by Oxygen Functional Groups. *J. Phys. D: Appl. Phys.* **2017**, *50*, 385305.

(16) Meng, Z.; Soler-Crespo, R. A.; Xia, W.; Gao, W.; Ruiz, L.; Espinosa, H. D.; Keten, S. A Coarse-Grained Model for the Mechanical Behavior of Graphene Oxide. *Carbon* **2017**, *117*, 476−487.

(17) Vinod, S.; Tiwary, C. S.; Machado, L. D.; Ozden, S.; Cho, J.; Shaw, P.; Vajtai, R.; Galvão, D. S.; Ajayan, P. M. Strain Rate Dependent Shear Plasticity in Graphite Oxide. *Nano Lett.* **2016**, *16*, 1127−1131.

(18) Hu, K.; Tolentino, L. S.; Kulkarni, D. D.; Ye, C.; Kumar, S.; Tsukruk, V. V. Written-in Conductive Patterns on Robust Graphene Oxide Biopaper by Electrochemical Microstamping. *Angew. Chem., Int. Ed.* **2013**, *52*, 13784−13788.

(19) Luo, C.; Yeh, C. N.; Baltazar, J. L.; Tsai, C.; Huang, J. A Cut-and-Paste Approach to 3D Graphene-Oxide-Based Architectures. *Adv. Mater.* **2018**, *30*, 1706229.

(20) Soler-Crespo, R. A.; Gao, W.; Mao, L.; Nguyen, H. T.; Roenbeck, M. R.; Paci, J. T.; Huang, J.; Nguyen, S. T.; Espinosa, H. D. The Role of Water in Mediating Interfacial Adhesion and Shear Strength in Graphene Oxide. *ACS Nano* **2018**, *12*, 6089−6099.

(21) Rahman, M.; Brazel, C. S. The Plasticizer Market: An Assessment of Traditional Plasticizers and Research Trends to Meet New Challenges. *Prog. Polym. Sci.* **2004**, *29*, 1223−1248.

(22) Zhang, M.; Huang, L.; Chen, J.; Li, C.; Shi, G. Ultratough, Ultrastrong, and Highly Conductive Graphene Films with Arbitrary Sizes. *Adv. Mater.* **2014**, *26*, 7588−7592.

(23) Liu, L.; Niu, Z.; Zhang, L.; Zhou, W.; Chen, X.; Xie, S. Nanostructured Graphene Composite Papers for Highly Flexible and Foldable Supercapacitors. *Adv. Mater.* **2014**, *26*, 4855−4862.

(24) Peng, L.; Xu, Z.; Liu, Z.; Guo, Y.; Li, P.; Gao, C. Ultrahigh Thermal Conductive Yet Superflexible Graphene Films. *Adv. Mater.* **2017**, *29*, 1700589.

(25) Tschaetsch, H. *Metal Forming Practice: Processes, Machines, Tools*; Springer-Verlag: Berlin Heidelberg, 2006.

(26) Kalia, S.; Dufresne, A.; Cherian, B. M.; Kaith, B. S.; Avérous, L.; Njuguna, J.; Nassiopoulos, E. Cellulose-Based Bio- and Nano-composites: A Review. *Int. J. Polym. Sci.* **2011**, *35*, 837875.

(27) Valentini, L.; Cardinali, M.; Fortunati, E.; Torre, L.; Kenny, J. M. A Novel Method to Prepare Conductive Nanocrystalline Cellulose/Graphene Oxide Composite Films. *Mater. Lett.* **2013**, *105*, 4−7.

(28) Fang, Q.; Zhou, X.; Deng, W.; Zheng, Z.; Liu, Z. Freestanding Bacterial Cellulose-Graphene Oxide Composite Membranes with High Mechanical Strength for Selective Ion Permeation. *Sci. Rep.* **2016**, *6*, 33185.

(29) Li, Y.; Zhu, H.; Shen, F.; Wan, J.; Han, X.; Dai, J.; Dai, H.; Hu, L. Highly Conductive Microfiber of Graphene Oxide Templated Carbonization of Nanofibrillated Cellulose. *Adv. Funct. Mater.* **2014**, *24*, 7366−7372.

(30) Betterman, L. R.; Ouyang, C.; Shah, S. P. Fiber-Matrix Interaction in Microfiber-Reinforced Mortar. *Adv. Cem. Based Mater.* **1995**, *2*, 53−61.

(31) Carrasco, P. M.; Montes, S.; García, I.; Borghei, M.; Jiang, H.; Odriozola, I.; Cabañero, G.; Ruiz, V. High-Concentration Aqueous Dispersions of Graphene Produced by Exfoliation of Graphite Using Cellulose Nanocrystals. *Carbon* **2014**, *70*, 157−163.

(32) Yang, W.; Zhao, Z.; Wu, K.; Huang, R.; Liu, T.; Jiang, H.; Chen, F.; Fu, Q. Ultrathin Flexible Reduced Graphene Oxide/Cellulose Nanofiber Composite Films with Strongly Anisotropic Thermal Conductivity and Efficient Electromagnetic Interference Shielding. *J. Mater. Chem. C* **2017**, *5*, 3748−3756.

(33) Shih, C.; Lin, S.; Sharma, R.; Strano, M. S.; Blankschtein, D. Understanding the pH-Dependent Behavior of Graphene Oxide Aqueous Solutions: A Comparative Experimental and Molecular Dynamics Simulation Study. *Langmuir* **2012**, *28*, 235−241.

(34) Kashyap, S.; Mishra, S.; Behera, S. K. Aqueous Colloidal Stability of Graphene Oxide and Chemically Converted Graphene. *J. Nanopart.* **2014**, *2014*, 640281.

(35) Jawaid, M.; Boufi, S.; Khalil, A. *Cellulose-Reinforced Nanofibre Composites: Production, Properties and Applications*; Elsevier: Duxford, 2017.

(36) An, Z.; Compton, O. C.; Putz, K. W.; Brinson, L. C.; Nguyen, S. T. Bio-Inspired Borate Cross-Linking in Ultra-Stiff Graphene Oxide Thin Films. *Adv. Mater.* **2011**, *23*, 3842−3846.

(37) Chen, M.; Chen, J.; Zhou, W.; Xu, J.; Wong, C.P. High-Performance Flexible and Self-Healable Quasisolid-State Zinc-Ion Hybrid Supercapacitor Based on Borax-Crosslinked Polyvinyl Alcohol/Nanocellulose Hydrogel Electrolyte. *J. Mater. Chem. A* **2019**, *7*, 26524−26532.

(38) Wicklein, B.; Kocjan, D.; Carosio, F.; Camino, G.; Bergström, L. Tuning the Nanocellulose-Borate Interaction to Achieve Highly Flame Retardant Hybrid Materials. *Chem. Mater.* **2016**, *28*, 1985−1989.

(39) Gardner, D. J.; Oporto, G. S.; Mills, R.; Samir, M. A. Adhesion and Surface Issues in Cellulose and Nanocellulose. *J. Adhes. Sci. Technol.* **2008**, *22*, 545−567.

(40) Liu, S.; Hu, K.; Cerruti, M.; Barthelat, F. Ultra-Stiff Graphene Oxide Paper Prepared by Directed-Flow Vacuum Filtration. *Carbon* **2020**, *158*, 426−434.